Composite Structures 329 (2024) 117794

Contents lists available at ScienceDirect

Composite Structures

journal homepage: www.elsevier.com/locate/compstruct

Probabilistic aeroelastic analysis of high-fidelity composite aircraft wing with manufacturing variability

Michael McGurk [a,*], Olivia Stodieck [b], Jie Yuan [a,c]

[a] Department of Mechanical and Aerospace Engineering, University of Strathclyde, Glasgow, G1 1XJ, UK
[b] Dapta Ltd., Bristol, BS1 1LT, UK
[c] Department of Aeronautics and Astronautics Engineering , University of Southampton, Southampton, SO17 1BJ, UK

ARTICLE INFO

Keywords:
Aeroelasticity
Flutter
Uncertainty quantification
Surrogate model
Composites
Global sensitivity analysis

ABSTRACT

Safety margins of aerospace structures can be improved through altering the laminate parameters of composite materials to increase flutter and divergence velocities. Existing work demonstrates the impact of material uncertainties on low-fidelity structural models that are not sufficient to represent realistic aircraft designs. A gap exists in quantifying laminate parameter uncertainties on aeroelasticity for high-fidelity three-dimensional composite structures in realistic tailored designs. This paper puts forward an efficient methodology for uncertainty quantification on the aeroelastic characteristics of three-dimensional composite structures using FE-based parametric composite models and advanced Kriging surrogate models. The methodology is tested on both low and high fidelity case studies to represent the composite wing structure. Similarities between the case studies are observed in the coefficient of variance of all hard flutter modes being within 0.15-1.4% of each other. The difference was found for divergence and soft flutter velocities where the coefficient of variance could be over ten times higher in the high fidelity case. Global sensitivity results revealed similar physical behavior cases can be produced from both studies at early design stages.

1. Introduction

Composite materials offer several useful characteristics such as high specific strength and tailorable stiffness that can be effectively exploited to improve efficiency in the design of aerospace structures. They can therefore significantly contribute to the UN goal of net-zero aircraft emissions by 2050 by reducing aircraft weight [1]. The introduction of aircraft based on composite architecture has been estimated to contribute 20%–25% of industry CO_2 reductions targets [2]. A crucial factor to consider in novel aircraft architectures is the interaction between aerodynamic and structural forces in a flexible structure, known as aeroelasticity. This is particularly important in the use of composite materials, which typically increase the flexibility of structures. Aeroelastic phenomena are divided into two main categories, static and dynamic. Static aeroelasticity accounts for the non-oscillatory behavior of aerodynamic interactions with flexible structures. The key static phenomenon is called “divergence” where aerodynamic force can overcome the structural stiffness beyond a certain velocity leading to a structural failure. The oscillatory aeroelastic behavior is referred to as dynamic aeroelasticity. An often disastrous impact of dynamic aeroelasticity is flutter, where, past a certain velocity, the structural response to a perturbation of aerodynamical excitation is negatively damped oscillations [3]. Both of the aeroelastic phenomena can lead to catastrophic structural failure, as in the case of Braniff International Airways Flight 542 [4].

As a result, stability boundaries related to aeroelastic qualities, namely divergence and flutter velocity, must be carefully considered during the early design stage of a novel aircraft. A recent work [5] has shown that the layup of composite structures has a significant impact on these aeroelastic behaviors through the change of structural stiffness that has been exploited extensively to improve aeroelastic qualities [6–9]. Discussed by Zheng and Wang [10], studies on aeroelasticity are mainly focused on deterministic divergence and flutter analysis without consideration of uncertainties in material properties.

However, being dependent on interactions between structure and aerodynamics where uncertainties do exist these material parameters are inherently uncertain. In composite manufacturing specifically, uncertainties can arise from several different sources such as material variability and tolerance of manufacturing processes [11,12]. Composite plates that are employed in the manufacture of aircraft wings are made up of layers of plies where fibers within an individual ply are orientated in a specific direction. Altering the ply orientation angle in subsequent ply has an impact on the stiffness of a material, hence the

* Corresponding author.
E-mail addresses: michael.mcgurk@strath.ac.uk (M. McGurk), j.yuan@soton.ac.uk (J. Yuan).

https://doi.org/10.1016/j.compstruct.2023.117794
Received 3 April 2023; Received in revised form 8 November 2023; Accepted 4 December 2023
Available online 6 December 2023

aeroelastic characteristics. It is widely recognized that the process of stacking plies has a significant degree of uncertainties that have been estimated in recent works to be ±5° in the form of uniform distributions [13,14]. These uncertainties can come from both human and machine processing causing misalignment in layers [15] and plies being dropped or damaged [16,17]. Uncertainty in ply orientation has been extensively researched, particularly in the case of buckling analysis, where it has been shown robust designs outperform deterministic designs under real-world situations that include uncertainties [18]. Scarth et al. [6] demonstrated the effectiveness of using Polynomial Chaos Expansion (PCE) with ply angle uncertainty with a flat composite plate case. Limitations were found in reduced improvement in computation time in cases where multiple modes entered flutter. It is possible for separate modes to enter flutter with different intensities. Furthermore, the mode coupling using the composite plate model is limited due to the relatively simple geometry considered in the flat plate model. Models with detailed geometry describing wing thickness are inherently more accurate in describing complex geometry. However, there are very few studies looking into the impact of ply orientation uncertainty on aeroelastic phenomena in high-fidelity three-dimensional test case due to the high computational cost and complexities of the development of numerical models.

High-fidelity structure models are typically constructed manually through Finite Element Modeling (FEM) with the aid of Computer Aided Design (CAD) software. In the early design stages, frequent updates of parameters such as ply layup are required, which is time-consuming when manually constructing CAD models. This is even more computationally expensive when in attempting to quantify the influence of uncertainties where thousands of variations of a structure would be required for Monte Carlo Simulations (MCS). The complexities however can be mitigated by using a fully parametric FE model including material and geometrical parameters. The work carried out at Dapta Ltd. has already demonstrated how a fully parametric model can be implemented to effectively describe the static and dynamic behavior of a complex three-dimensional wing-box model [19]. This was achieved by linking parameter inputs with FEM pre-processors in the Python interface, allowing for a series of random inputs to generate corresponding outputs.

MCS has been commonly used to investigate the influence of material uncertainties on aeroelastic characteristics [13]. Although robust, MCS can often require a large number of samples to truly capture the possible behavior of the system, and for this reason, it is mainly used to validate alternative approaches. As mentioned previously, PCE is implemented to reduce the computational expense of MCS for composite case studies [6]. Previous work has demonstrated the effectiveness of implementing surrogate models to aid in MCS with complex models, particularly in some highly complex cases such as aeroelastic analysis which can be time-consuming even for a single run [20–22]. With effectively gathered limited training data from high fidelity simulations, it is possible to construct these surrogate models through several methods such as PCE [23,24] and Gaussian process models [25–27]. Yan et al. [28] proposed the use of a Kriging surrogate model to sample probability density functions of updated parameters integrated with a Bayesian interface. When paired with Latin-Hypercube sampling to gather training data, it has been shown that advanced Kriging methods provide accurate surrogate models from relatively low amount of data. Liu et al. [29] developed a sophisticated surrogate model for the purpose of quantifying interval uncertainties in structures. A methodology for pairing Latin-Hypercube Sampling with Kriging methods in a sequential process was demonstrated as opposed to preselected training data, showing improved accuracy over alternative approaches for nonlinear dynamical systems.

Latin-Hypercube Sampling (LHS) first described by McKay in 1979 [30] is commonly used as a sampling technique during the surrogate model development. LHS with least-squares linear regression can significantly reduce the number of samples required compared to Monte Calo Techniques [6]. It has been recently adopted for the study of Uncertainty Quantification (UQ) and optimization in composite laminate properties to investigate the impact of ply angle uncertainty and ply thickness on both static and dynamic properties [14,31,32]. The relative importance of each input on uncertainty through global sensitivity analysis has not been investigated. Sobol indices, first introduced by Sobol [33,34] can be used to indicate the relative sensitivity of parameters [35]. Saltelli details an effective sampling algorithm to determine Sobol indices that are integrated into OpenTURNS software implemented in this study [36,37]. Although effective, it has not been applied to aeroelastic systems.

The objective of this work is to quantify the influence of ply angle uncertainties in the static and dynamic aeroelastic behavior of a composite wing. The main contribution of this paper is to apply a UQ methodology in couple with Kriging-based surrogate models to a high-fidelity three-dimensional aeroelastic system. An advanced Kriging method paired with Latin-hypercube sampling is utilized in the development of surrogate models to improve computational efficiency. A global sensitivity analysis is performed using Sobol indices to identify the most influential parameters. The methodology of UQ is first validated by using a flat composite plate test case before being applied to an aerofoil-shaped parametric wing box model for aeroelastic analysis. Results from the flat plate wing box case study will be also used to compare that from the aerofoil shaped wing box case study to indicate the limitation of the flat plate model.

2. Methodology

The section will present the general methodology used in both low and high-fidelity case studies. A brief overview of aeroelastic analysis techniques and general laminate theory will be first presented. Then, the methodology of uncertainty quantification applied to both case studies will be described, including surrogate model development and global sensitivity analysis.

2.1. Aeroelastic analysis

The aeroelastic analysis laid out here is based on mathematical models that can be arranged into the second-order differential equation shown in Eq. (1). Once in this form, both divergence and flutter velocities can be determined. Aeroelastic systems can be arranged in this form assuming structural forces acting to balance aerodynamic forces.

$$\hat{\mathbf{M}}\ddot{q} + \hat{\mathbf{K}}q = \rho_{air}V\hat{\mathbf{B}}\dot{q} + \rho_{air}V^2\hat{\mathbf{C}}q \tag{1}$$

where q denotes the system's degrees of freedom (displacement vector) and $\hat{\mathbf{M}}$ and $\hat{\mathbf{K}}$ are the structural mass and stiffness matrices respectively. Matrices $\hat{\mathbf{B}}$ and $\hat{\mathbf{C}}$ account for aerodynamic forces (lift and drag) and the resulting moments, which are dependent on airspeed. Terms related to air-speed and -density are commonly divided from constant structural matrices in aeroelastic analysis to simplify analysis. Each matrix is of the size $N \times N$ where N is the number of degrees of freedom of the system. The standard differential equation can be rearranged into first-order state Eq. (2) as:

$$\dot{\mathbf{q}} = \mathbf{Q}\mathbf{q} \tag{2}$$

where:

$$\mathbf{q} = \begin{bmatrix} \dot{q} \\ q \end{bmatrix} \qquad \mathbf{Q} = \begin{bmatrix} \rho_{air}V\hat{\mathbf{M}}^{-1}\hat{\mathbf{B}} & \hat{\mathbf{M}}^{-1}(\rho_{air}V^2\hat{\mathbf{C}} - \hat{\mathbf{K}}) \\ I_{N\times N} & 0_{N\times N} \end{bmatrix}$$

Matrix $\mathbf{Q}$ will be referred to as the linear matrix as it fully captures the linear behavior of the system.

Divergence is defined as the point where static aerodynamic forces are equal to structural restoring forces, defined in Eq. (3). Matrix $\hat{\mathbf{C}}$ being dependent on velocity, divergence velocity V_d can be determined

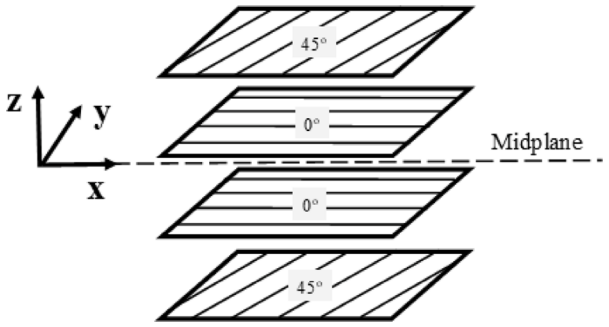

Fig. 1. [45/0/]s laminate.

through computing the determinant of Eq. (3) and solving for V_d [38].

$$\hat{\mathbf{K}} = \rho_{air} V_d \hat{\mathbf{C}} \tag{3}$$

Flutter velocity is the point where the system becomes undamped. The damping ratio for each mode can be found through the classical eigenvalue problem writing Eq. (2) as $\dot{\mathbf{q}} - \mathbf{Q}\mathbf{q} = 0$. Assuming a oscillatory response $q = q_o e^{\psi_i t}$ the eigenvalue problem is written:

$$\left[\mathbf{Q} - \mathbf{I}\psi_i\right]\phi = 0 \tag{4}$$

where ψ_i are eigenvalues in the conjugate pair

$$\psi_i = -\zeta_i \omega_i \pm i\omega_i \sqrt{1-\zeta_i} \tag{5}$$

where ω_i are the aeroelastic frequencies and ζ_i are the damping ratios [39]. These frequencies are related to the aeroelastic modes of the system and are not to be confused with the structural modes. Matrix ϕ contains the corresponding eigenvectors. Flutter is characterized by unstable negatively damped oscillations. From this definition, it can be determined that if any of the real parts of Eq. (5) are positive, the system is dynamically unstable [3]. A mode can enter flutter in two forms, "soft flutter" and "hard flutter". Soft flutter behavior occurs when damping ratio of a mode gradually becomes negative with a shallow gradient as velocity increases. This can lead to a behavior known as "hump mode". As stated by Wright and Cooper. [3] a hump mode can often become stable again at higher velocities and may be possible to counteract with small structural damping modifications. In contrast, when a mode enters a hard flutter a steep gradient of damping ratio with velocity is observed.

2.2. Laminate theory

A laminate as discussed in this work is an organized stack of composite plies with uni-directional fiber direction angles. Two constraints were placed on the laminate stacking sequence based on common industrial practices. The laminate must be symmetrical in the z-midplane and ply angle can only be in four directions 0°, +45°, −45° and 90°. Fig. 1 shows a laminate of lay-up [45/0/0/45], which is denoted simply as [45/0/]s, where the index s refers to symmetry.

Elastic properties of the entire laminate are defined by the 6 × 6 **ABD** matrix, which is obtained with knowledge of applied loads and material properties [40]. The transformed reduced stiffness matrix $\mathbf{Q}^*_{ij}$ for each ply (defined in Appendix A) which is dependent on θ is implemented to determined **ABD** in Eqs. (6).

$$\begin{aligned}
\mathbf{A}_{ij} &= \sum_{k=1}^{n} \left[\mathbf{Q}^*_{ij}\right]_k \left(z_k - z_{k-1}\right) \\
\mathbf{B}_{ij} &= \frac{1}{2}\sum_{k=1}^{n} \left[\mathbf{Q}^*_{ij}\right]_k \left(z_k^2 - z_{k-1}^2\right) \\
\mathbf{D}_{ij} &= \frac{1}{3}\sum_{k=1}^{n} \left[\mathbf{Q}^*_{ij}\right]_k \left(z_k^3 - z_{k-1}^3\right)
\end{aligned} \tag{6}$$

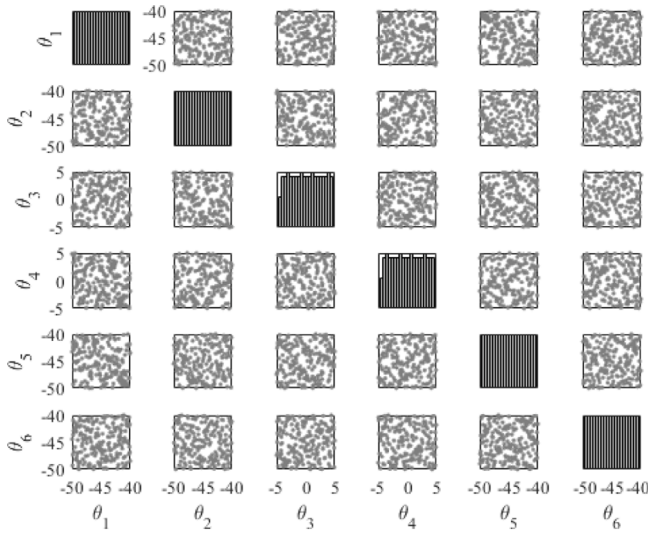

Fig. 2. Scatter graph and histograms of ply orientation angle with 100 samples for the layup [−45, −45, 0]s.

where z_k represents the distance from the midplane to bottom of kth ply. Noting $\mathbf{Q}^*_{ij}$ is different for each ply whilst direct strains ϵ and curvatures κ will be the same, following integration across the total thickness, a structural restoring moment can be calculated in Eq. (7). Through this relationship impact of the laminate layup is linked to structural response.

$$\begin{pmatrix} M_{xx} \\ M_{yy} \\ M_{xy} \end{pmatrix} = \begin{bmatrix} \mathbf{B}_{11} & \mathbf{B}_{12} & \mathbf{B}_{16} \\ \mathbf{B}_{12} & \mathbf{B}_{22} & \mathbf{B}_{26} \\ \mathbf{B}_{16} & \mathbf{B}_{26} & \mathbf{B}_{66} \end{bmatrix} \begin{pmatrix} \epsilon^o_{xx} \\ \epsilon^o_{yy} \\ \gamma^o_{xy} \end{pmatrix} + \begin{bmatrix} \mathbf{D}_{11} & \mathbf{D}_{12} & \mathbf{D}_{16} \\ \mathbf{D}_{12} & \mathbf{D}_{22} & \mathbf{D}_{26} \\ \mathbf{D}_{16} & \mathbf{D}_{26} & \mathbf{D}_{66} \end{bmatrix} \begin{pmatrix} \kappa^o_{xx} \\ \kappa^o_{yy} \\ \kappa^o_{xy} \end{pmatrix} \tag{7}$$

Due to symmetry, it can be observed from Eq. (6) that all values of **B** will be zero. In a symmetric matrix, it can therefore be deduced that structural stiffness is largely dependent on **D** which is derived from both laminate properties and layup. Restoring moments in both case studies are used to generate the $\hat{\mathbf{K}}$ in Eq. (1), linking laminate properties to aeroelastic characteristics.

2.3. Uncertainty quantification

A six-ply laminate will be considered in both test cases in this paper. Each ply is treated as an independent variable so in quantifying uncertainty in ply orientation angle there are six uncertain parameters to consider. Following methodology from Dodwell et al. [13] uniform distributions that extend ±5° past nominal θ will be selected for each ply orientation angle describing uncertainties observed in manufacturing. From these distributions, samples were gathered through MCS to achieve an efficient spread of data shown in Fig. 2 as an example. For each input, an output sample for either divergence or flutter velocity is generated through the aeroelastic analysis. 95% confidence bands can be plotted with the resulting Probability Density Function (PDF) of full statistical MCS output [35]. The Coefficient of variance ($COV = \frac{\sigma}{\mu}$) is then used to determine the normalized statistical variation of a prediction.

2.3.1. Global sensitivity analysis

The sampling method laid out by Saltelli is implemented for global sensitivity analysis [36], refereed to as Sobol analysis. This method

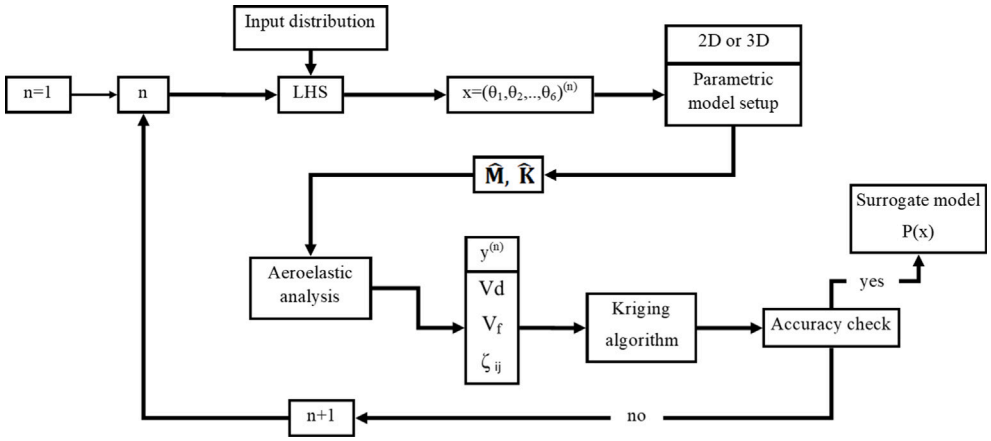

Fig. 3. Surrogate model development.

analyses the influence random inputs have on outputs in a system with multiple inputs [33]. First order Sobol indices quantify the influence each individual input has on the output when considering uncertainty. Two sets of input samples are required $X^{(1)}$ and $X^{(2)}$ where $x = [\theta_1, \theta_2, \ldots, \theta_6]$, $X = \left\{x^{(1)}, x^{(2)}, \ldots, x^{(n)}\right\}$ and n is sample size. The estimation of first order indices considering the impact of a random vector on random variable Y^k consists in estimating the quantity

$$V_i = \mathrm{Var}\left[\mathbb{E}\left[Y^k|X_i\right]\right] = U_i - \mathbb{E}\left[Y^k\right]^2 \tag{8}$$

where Sobol proposes to estimate quantity $U_i = \mathbb{E}\left[\mathbb{E}\left[Y^k|X_i\right]^2\right]$ by swapping every variable in the two samples apart from X_i through a call function

$$\hat{U}_i = \frac{1}{N}\sum_{k=1}^{N} Y^k\left(\theta_{k1}^{(1)}, \ldots, \theta_{k(i-1)}^{(1)}, \theta_{ki}^{(1)}, \theta_{k(i+1)}^{(1)}, \ldots, \theta_{k6}^{(1)}\right) \times Y^k\left(\theta_{k1}^{(2)}, \ldots, \theta_{k(i-1)}^{(2)}, \theta_{ki}^{(2)}, \theta_{k(i+1)}^{(2)}, \ldots, \theta_{k6}^{(2)}\right) \tag{9}$$

The first order Sobol indices are then estimated by

$$\hat{S}_i = \frac{\hat{U}_i - \mu^2}{\hat{\sigma}^2} \tag{10}$$

Taking μ and $\hat{\sigma}$ as the mean and standard deviation of Y_k. Total order indices $\hat{S}_{Ti}$, consider interactions between the different inputs and their influence on the output [41].

$$\hat{S}_{Ti} = \hat{S}_i + \sum_{j=1, j\neq i}^{n} \hat{S}_{ij} \tag{11}$$

where

$$\hat{S}_{ij} = \frac{\mathrm{Var}\left[\mathbb{E}\left[Y^k|X_i, X_j\right]\right]}{\hat{\sigma}^2} \tag{12}$$

2.4. Surrogate model development

A Kriging algorithm is used for the development of surrogate models to improve the computational efficiency of the UQ process. Separate models are required for individual modes in each laminate layup due to varying behavior. In Kriging, the best linear unbiased estimator estimates an unknown random process mean [42]. In the case of divergence velocity V_d, the aim is to generate a predictor P that estimates V_d based on inputs for each ply lay up $x = [\theta_1, \theta_2, \ldots, \theta_6]$ so $V_d = P(x)$. Sets of training input data $X = \left[x^{(1)}, x^{(2)}, \ldots, x^{(n)}\right]$ and corresponding outputs $Y = \left[y^{(1)}, y^{(2)}, \ldots, y^{(n)}\right]$ are gathered first [43]. As is common Kriging is frequently paired with LHS also used for UQ in Section 2.3 to gather training data. This method ensures a diverse set of points along all variables. The Kriging predictor is formulated as follows

$$P(x) = \mu(x) + \mathbf{w}^T(x)\mathrm{K}^{-1}(Y - \mu(X)) \tag{13}$$

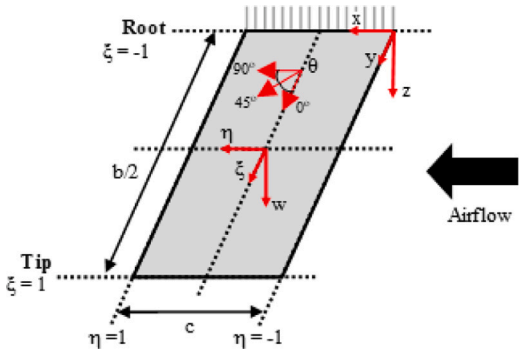

Fig. 4. A cantilever flat plate wing box model.

where $\mu(x)$ is the mean function that represents the expected value or trend of the response variable. It is typically assumed to be constant or can be defined based on prior knowledge or domain expertise. Covariance matrix K is an $n \times n$ matrix where $K_{ij} = Corr[x^i, x^j]$ represents the covariance or correlation between ith and jth input points. The weight factor $\mathbf{w}(x)$ is defined as

$$\mathbf{w}(x) = \mathrm{K}^{-1}Corr[x, X] \tag{14}$$

where $Corr[x, X]$ is a vector representing the correlation or covariance between input x and training point X. Accuracy of P is computed with comparison to a separate set of test data.

Fig. 3 demonstrates the development of a surrogate model for both cases. Statistical distributions are defined for input parameters $[\theta_1, \theta_2, \ldots, \theta_6]$ where LHS samples are drawn. These distributions are defined to capture all possible inputs the surrogate model is expected to experience. Aeroelastic analysis with a low and high-fidelity model is then performed for each generated sample input. The corresponding outputs are then used in the construction of Kriging surrogate model. The accuracy of the model is checked against separate test data to ensure its convergence. Training data is gathered until accuracy of the model is converges with additional training data.

3. Flat plate wing box case

In this section, a flat plate wing box case is presented which is used to validate the methodology of the aeroelastic analysis and UQ including surrogate modeling techniques. First, flat plate aeroelastic model based on a composite plate is presented; then both deterministic and probabilistic results are described and discussed.

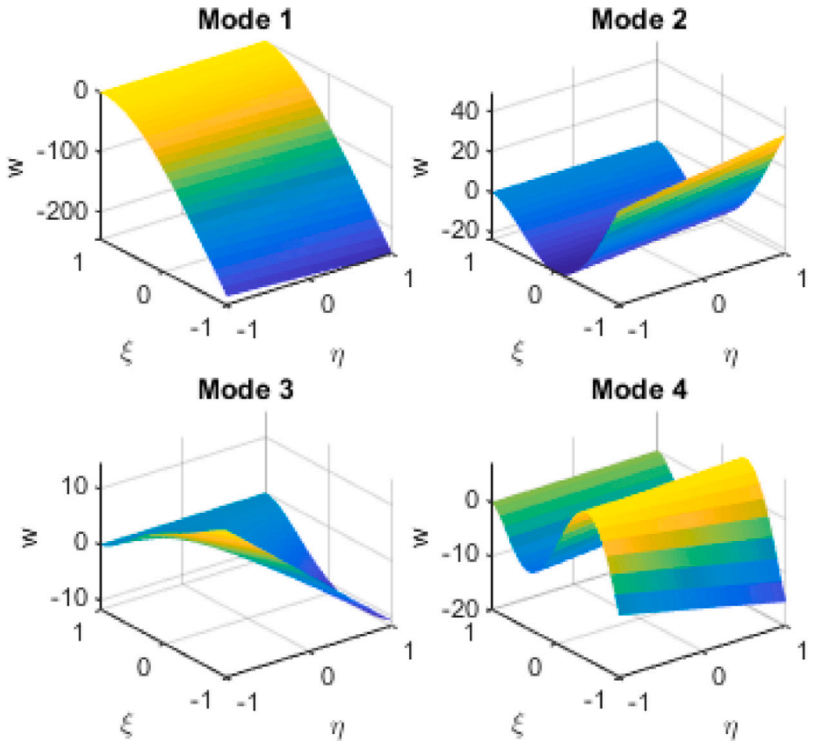

Fig. 5. Mode shapes for flat plate case study.

Table 1
Parameters and material properties for flat plate case study.

Parameter	Value
Number of plies (n)	6
Span (b)	2 m
Chord (c)	0.5 m
Ply thickness (t)	1.7 mm
Longitudinal Young's modulus (E_{11})	128 GPa
Transverse Young's modulus (E_{22})	11 GPa
Shear modulus (G_{12})	11 GPa
Poisson's ratio (ν_{12})	0.28

3.1. Model setup

Fig. 4 shows a simple cantilever beam considered as the flat plate model in this work. A six-ply symmetric layup was used with parameters in Table 1 describing the dimensions of the wing. Examination of ply orientation angle θ in reference to Fig. 4 shows 90° plies counteract wing twist and 0° plies counteract bending. As is commonly practiced in simplified models, chordwise rigidity was assumed. This means there is only one out of plane twist mode. The chordwise shape remains straight but has the freedom to move at $\eta = -1$ and $\eta = 1$. It is possible to derive mass and stiffness matrix ($\hat{\mathbf{M}}$ and $\hat{\mathbf{K}}$) through the energy method with assumed mode shapes [44]. Mode shapes are based on Legendre polynomials as it is similar to [45]. The general form of kinetic energy is taken:

$$E_k = \frac{1}{2}\iiint \rho\left[\dot{u}^2 + \dot{v}^2 + \dot{w}^2\right] dxdydz \tag{15}$$

Assuming energy associated with in-plane velocities is negligible, $\dot{u}$ and $\dot{v}$ can be excluded from Eq. (15) [46]. With a symmetric laminate, chordwise rigidity and neglecting energy due to in-plane deformations, strain energy can be found

$$E_s = \frac{1}{2}\iint \mathbf{D}_{11}\left(\frac{\partial^2 w}{\partial y^2}\right)^2 + 4\mathbf{D}_{16}\frac{\partial^2 w}{\partial y^2}\frac{\partial^2 w}{\partial x \partial y} + 4\mathbf{D}_{66}\left(\frac{\partial^2 w}{\partial x \partial y}\right)^2 dxdy \tag{16}$$

With relationships for E_k and E_s, the free vibration is derived based on the Lagrange equation for a conservative system $E_s + E_k = constant$

$$\frac{\partial\left(E_s + E_k\right)}{\partial t} = 0 \tag{17}$$

It has been shown in literature a solution can be found through a Rayleigh–Ritz approach [47]. Out-of-plane deflection w can be taken as the sum of assumed shape functions from Legendre Polynomials (defined in Appendix B) in the form

$$w(\xi,\eta) = \sum_{m=0}^{m_{max}}\sum_{n=0}^{n_{max}} q_{mn}\,(1+\xi)^2\,L_m(\xi)L_n(\eta) \tag{18}$$

where q_{mn} represents modal coordinates with index m representing spanwise mode and n chordwise. Implementing Eq. (18) in Eqs. (15) and (16), structural mass and stiffness matrices can be derived through energy balance:

$$\begin{aligned}\frac{d}{dt}\left(\frac{\partial E_k}{\partial \dot{q}_{ij}}\right) &= \hat{\mathbf{M}}\ddot{\mathbf{q}}\\ \frac{\partial E_s}{\partial q_{ij}} &= \hat{\mathbf{K}}\mathbf{q}\end{aligned} \tag{19}$$

The Lagrange equation is used to derive the aerodynamic matrices also, where incremental work along the wing is given by:

$$\delta W = \int_{wing}\left[dL\left(-\delta w\right) + dM\left(\delta\chi\right)\right] \tag{20}$$

where δw is incremental heave and $\delta\chi$ is incremental pitch. Quasi-steady strip theory aerodynamics are implemented due to the relatively low velocities and simple unswept geometry of the plate. Aerodynamic lift (dL) and moment (dM) for each strip is then given by

$$\begin{aligned}dL &= \frac{1}{2}\rho V^2 c a_w\left(\frac{\dot{w}}{V} + \chi\right)dy\\ dM &= \frac{1}{2}\rho V^2 c^2\left[ea_w\left(\frac{\dot{w}}{V} + \chi\right) + M_{\dot{\chi}}\left(\frac{\dot{\chi}c}{4V}\right)\right]dy\end{aligned} \tag{21}$$

Table 2
Deterministic results for flat plate case study. Featuring the divergence velocity and the lowest flutter velocity.

Layup	V_d [m/s]	V_f [m/s]	ω [Hz]
[45, 45, 0] s	57.48	59.94	17.30
[90, 90, 0] s	79.60	12.26	9.40
[−45, −45, 0] s	259.76	124.32	17.30
[0, 0, 45] s	101.62	67.12	15.71
[90, 90, 45] s	65.85	35.40	9.76
[−45, −45, 45] s	262.08	126.80	17.44
[0, 0, −45] s	110.53	66.61	15.71
[45, 45, −45] s	58.47	58.34	17.43
[90, 90, −45] s	97.54	41.34	9.76
[0, 0, 90] s	96.88	59.77	15.62
[45, 45, 90] s	51.65	51.63	17.26
[−45, −45, 90] s	261.31	118.04	17.25

where a_w is the effective lift curve slope which is assumed to be a function of span location y and 2D lift slope [48].

$$a_w = 2\pi\left(1 - \frac{y^3}{b}\right) \tag{22}$$

Unsteady pitch velocity term $\left(M_{\dot{\chi}} = -1.2\right)$ is introduced to account for reduced frequency effects. This term acts as an approximation to Theodorsen's function derivative based on an average over a range of reduced frequencies and flexural axis positions [49]. Implementing Lagrange polynomials aerodynamic matrices $\hat{\mathbf{B}}$ and $\hat{\mathbf{C}}$ are derived in Appendix B.

When determining flutter and divergence velocities, results converge with eight order Legendre polynomials, so in Eq. (18) when $n = 1$ and $m = 8$. The first four mode shapes for a $[-45, -45, 45]$s laminate as an example are shown in Fig. 5. Mode 1 and 2 are the first and second spanwise bending. Mode 3 is the first twisting mode while mode 4 is a coupled third spanwise bending and twisting mode.

3.2. Results

Deterministic results for divergence, lowest flutter velocity and structural frequency (ω) without material uncertainly are displayed in Table 2. Flutter velocity is initially taken as the lowest velocity where the damping ratio of any mode becomes negative, to obtain a general idea of stability before examining specific modes. It shows that both divergent and flutter speed varies significantly with the layout of fiber angle orientation. This can be explained through the impact of laminate layup on the structural stiffness matrix which in turn affects aeroelastic characteristics. Typically, higher structural stiffness results higher natural frequency for a structure. Table 2 shows some correlation between ω and divergence and flutter speed, with higher ω resulting in higher V_d and V_f. However, this does not hold true in all cases as observed in $[45, 45, 0]$s layup with a relatively high natural frequency but low divergence and flutter velocity. As a result, assumptions of aeroelastic characteristic cannot be made purely on structural stiffness. Laminates with outer ply angles of −45° were shown to give divergence speed over double the closest alternative and flutter speed an increase of over 70%.

In every case mode 1 diverges at the lowest velocity, shown at V_d in Table 2. This is the first bending mode shown in Fig. 5. Typically in wings divergence is dominated by torsion [3]. In this case an untapered wing is considered, and the strip theory aerodynamic model assumes uniform lift throughout the span but resistance to bending is lower at the tip. Generally, untapered wings also have higher torsional stiffness and weaker coupling between bending and torsion [50]. Both modes 3 and 4 typically enter flutter, dependent on a layup in which the modal damping ratio becomes negative first. Damping ratio plots in Fig. 6 are obtained through eigenvalue analysis of the system's Q matrix. Examination of the damping ratio plot of mode 4 show a gradual decrease in damping ratio as the mode becomes dynamically unstable. This reveals soft flutter behavior often referred to as a "hump mode".

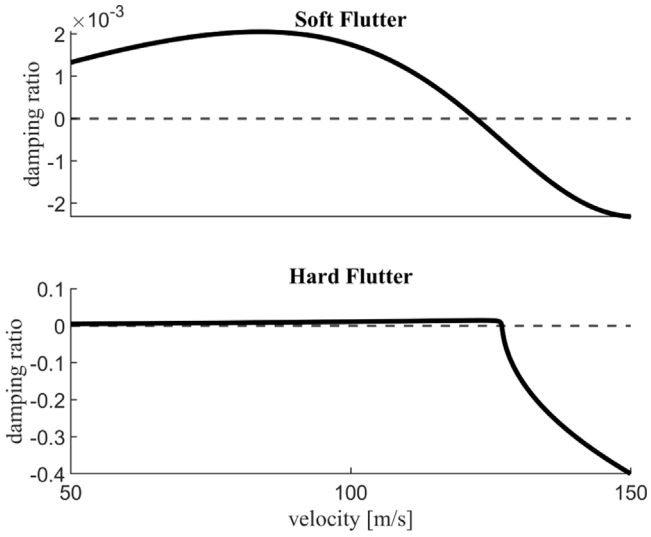

Fig. 6. Flutter modes.

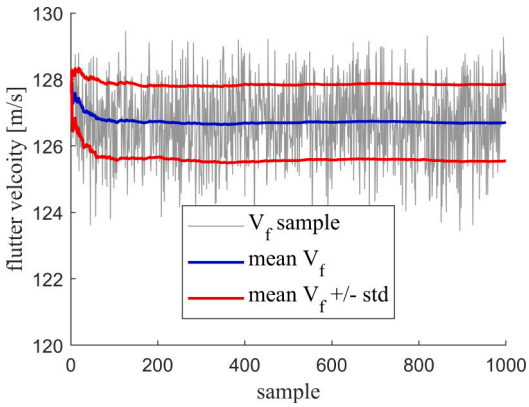

Fig. 7. Example convergence of samples for hard flutter in $[-45, -45, 45]$s.

Inversely, mode 3 enters flutter with a steep gradient, describing hard flutter behavior. A hard flutter mode becomes unstable suddenly and is challenging to counteract, modifications would act to shift the behavior to a higher velocity [51].

Fig. 6 shows the difference in damping ratio plots between soft and hard flutter for a $[-45, -45, 45]s$ layup. The type of flutter mode is identified through the sensitivity/gradient of the damping to the airspeed. A sharp decrease in damping ratio defines hard flutter and a gradual shows decrease soft flutter. In this scenario it is observed that hard and soft flutter velocity is reached within 5 m/s of each other. This suggests uncertainties in the fiber angles may significantly affect which flutter mode will appear at first.

As shown in Fig. 2, fiber angle uncertainty in a form of uniform distribution spanning ±5° from the nominal value is applied to each of six layers of the composite plate. MCS is performed for the uncertainty propagation until the mean value of the output distribution is converged. Fig. 7 provides an example of convergence plot for flutter speed, converging by 1000 samples. Divergence point is treated as a single output as the velocity when determinant of Eq. (3) is zero. Damping ratio plots are required to determine flutter mechanism for each mode. To distinguish between soft and hard flutter behavior surrogate models for damping behavior of both modes are produced. As a result, three times the amount of training data compared to divergence velocity is required. This is consistent with all other laminates investigated. Considering the fast computation of this model, MCS was done without the aid of surrogate models initially.

Table 3
Probabilistic results for flat plate wing box case study.

Layup	V_d		V_f	
	Mean [m/s]	COV [%]	Mean [m/s]	COV [%]
[45, 45, 0] s	57.78	0.97	57.78	1.70
[90, 90, 0] s	83.03	4.54	17.92	2.66
[−45, −45, 0] s	258.76	1.92	124.31	1.06
[0, 0, 45] s	101.08	4.24	68.80	1.59
[90, 90, 45] s	67.57	1.23	37.43	3.63
[−45, −45, 45] s	260.89	1.88	126.76	1.02
[0, 0, −45] s	111.13	7.97	68.22	1.81
[45, 45, −45] s	58.74	0.83	58.73	1.14
[90, 90, −45] s	99.77	1.19	42.37	1.26
[0, 0, 90] s	99.98	7.86	61.67	2.34
[45, 45, 90] s	52.03	1.25	51.97	0.77
[−45, −45, 90] s	260.14	0.78	118.13	0.82

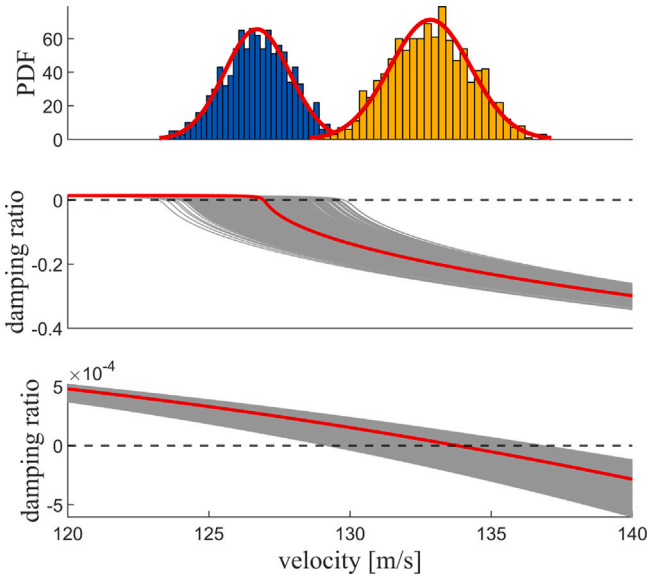

Fig. 8. [−45, −45, 45]s flat plate damping ratio.

Table 4
Parameters for aerofoil shaped wing box case study.

Parameter	Value
Number of plies (n)	6
Wingspan (b)	2 m
Wing chord (c)	0.2 m
Ply thickness (t)	0.2 mm
Spanwise elements	40
Chordwise elements	10
Material density	1520 kg/m^3
E_{11}	128 GPa
E_{22}	11 GPa
ν_{12}	0.28

Table 5
Deterministic results for aerofoil shaped wing box case study including flutter frequencies.

Layup	Structural frequency [Hz]	Soft flutter [m/s]	Hard flutter [m/s]	Divergence [m/s]
[−45, −45, 45] s	5.02	77.84 (30 Hz)	193.37 (118 Hz)	181.95
[0, 0, −45] s	10.15	107.73 (62 Hz)	96.43 (80 Hz)	178.33
[90, 90, 45] s	7.83	53.96 (25 Hz)	169.89 (97 Hz)	58.49

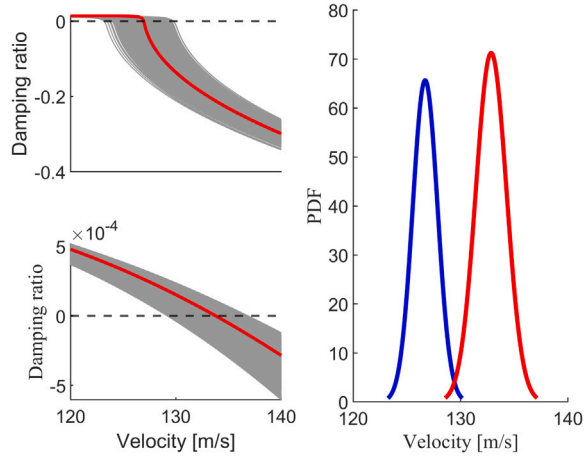

(a) Layup [-45, -45, 45]s

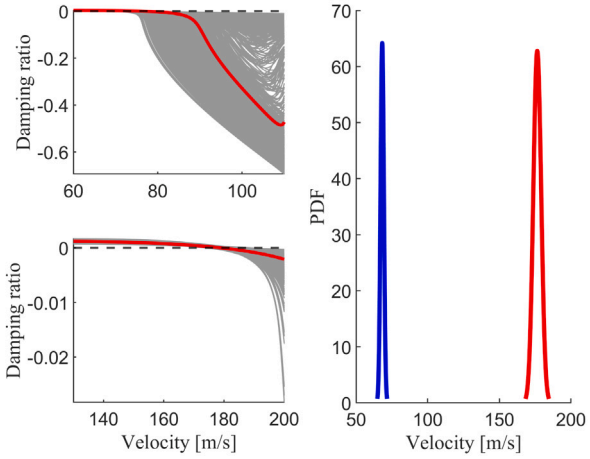

(b) Layup [0, 0, -45]s

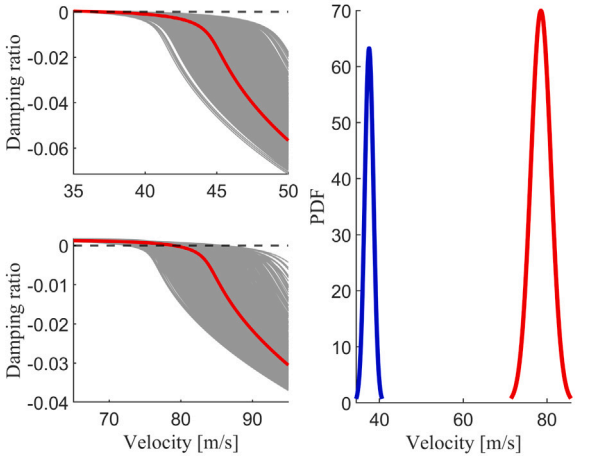

(c) Layup [90, 90, 45]s

Fig. 9. Damping ratio plots and PDF for flat plate wing box case study. (soft flutter –), (hard flutter –).

Table 3 shows results for divergence and lowest flutter velocity including Coefficient of Variance (**COV**) with material uncertainty. A pattern can be identified in the robustness of the divergence speed. Laminates containing 0° outer plies are up to four times less robust (in

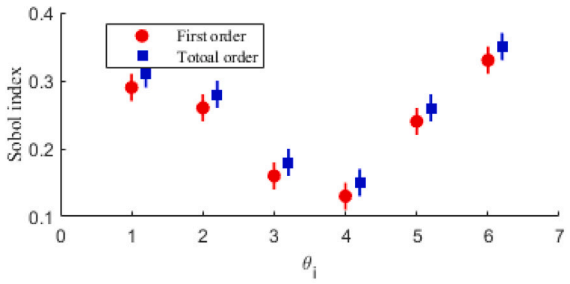

(a) Layup [-45, -45, 45]s

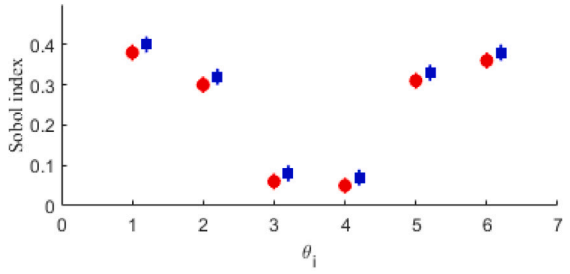

(b) Layup [0, 0, -45]s

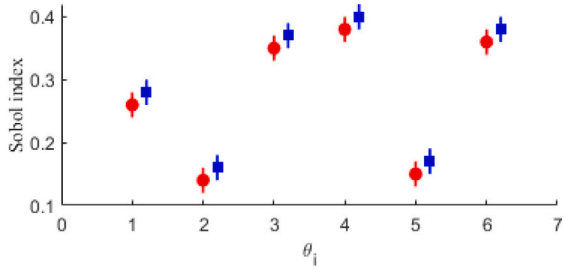

(c) Layup [90, 90, 45]s

Fig. 10. Sobol indices for divergence in flat plate wing box case study.

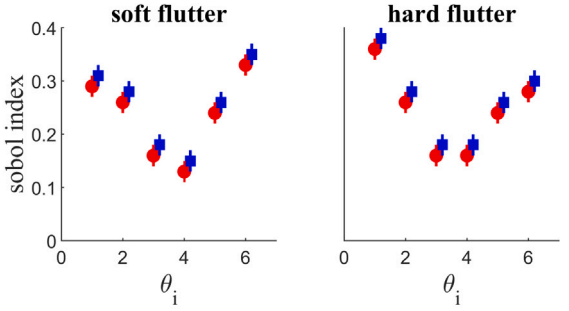

(a) Layup [-45, -45, 45]s

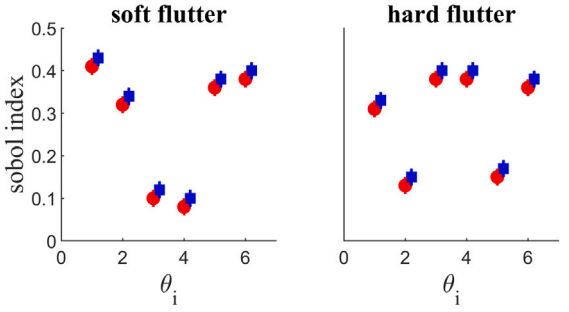

(b) Layup [0, 0, -45]s

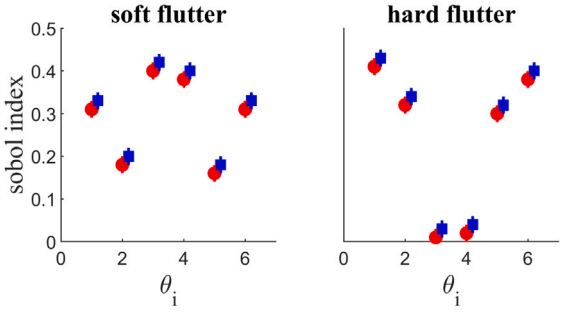

(c) Layup [90, 90, 45]s

Fig. 11. Sobol indices for flutter in flat plate wing box case study.

terms of COV) than the least robust layup without zero outer plies. It is more difficult to obtain a conclusion from the flutter results, likely due to different modes entering flutter depending on the layup. Closer examination is therefore required into the specific mechanism of flutter for certain laminates. The best-performing laminate considering both flutter velocity, divergence velocity and robustness is $[-45, -45, 45]$s. The least robust layup with respect to divergence $[0, 0, -45]$s and the least robust with respect to flutter $[90, 90, 45]$s. These three layups were selected to be investigated further with the aim of determining the reason for their respective robustness.

With the three laminates selected, Kriging surrogate models were built following the process in Fig. 3. A separate model is built for each behavior with data that is obtained from running eigenvalue analysis over a range of velocities. Divergence speed models only require inputs for each ply angle and corresponding outputs for divergence velocity. For both flutter modes, an array of damping ratio results with corresponding velocities are taken as inputs and outputs. The surrogate model can be then used to produce damping ratio plots determining flutter speed when the damping ratio crosses the x-axis. This is done specifically for the case of the "hump mode" to account for scenarios where a combination of inputs causes the mode to become stable again or not become unstable at all. An accurate surrogate model in this study was defined as less than 1% difference when compared to a separate set of comparison data. The compassion data set consisted of 100 samples taken independently though LHS. Using the sample inputs used to

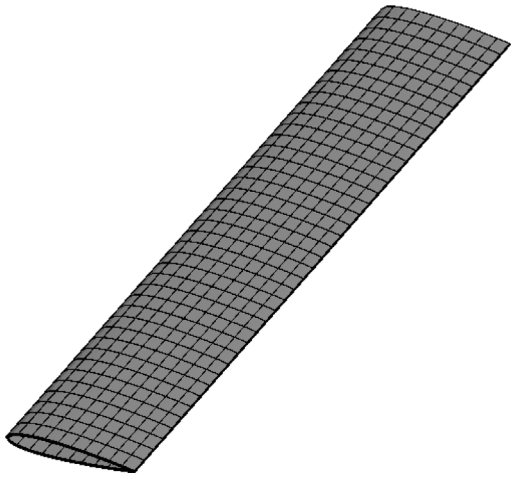

Fig. 12. A cantilever Wing box model.

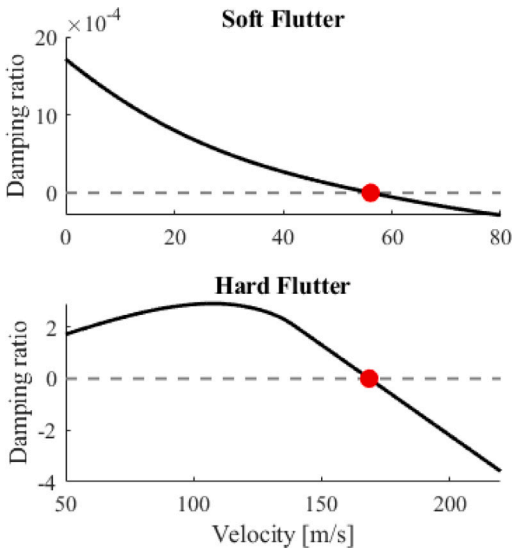

Fig. 13. Soft and hard flutter damping ratio plots for $[90, 90, 45]_S$ layup in aerofoil shaped wing box model.

gather the comparison data set with the surrogate model, accuracy of the results for divergence and flutter velocity was evaluated. In the flat plate wing box case study, it was found that an acceptable model can be obtained with training data from between 80–150 samples using LHS techniques.

The following results are obtained using surrogate models. Fig. 8 shows histograms of flutter velocity for both soft and hard flutter modes with damping ratio plots for 1000 MCS. Probability density functions (PDF) are displayed in Fig. 9. One can find out that there is a crossover area between the two modes. Physically, this means if a flutter occurs between $128 - 130$ m/s it could either be a soft or hard flutter.

Fig. 9 shows damping ratio plots and corresponding PDFs for $[0, 0, -45]_S$ and $[90, 90, 45]_S$ laminates. In both cases, hard flutter occurs first and there is no overlap between the modes. In an ideal scenario, soft flutter occur before the hard flutter, where damping ratio becomes negative gradually. The soft flutter can lead to low amplitude oscillations before the behavior becomes dangerous, which can be counteracted unlike the hard flutter [52]. However, in this study, it was found in Fig. 9 as well as in Fig. 15 that the hard flutter can take place at first for some layouts before the soft flutter, which make the design potentially more catastrophic. Global sensitivity analysis discussed in Section 2.3.1 is carried out with respect to divergence and flutter velocities for each layup to determine each orientations angle's impact on aeroelastic characteristics. Figs. 10 and 11 display the Sobol indices obtained for three fiber angle layouts namely $[-45, -45, 45]_S$, $[0, 0, -45]_S$ and $[90, 90, 45]_S$. In these layouts, "1" is the top ply while "6" is the bottom ply. Since divergence occurs in the first bending mode, the results in Fig. 10 can be explained. As mentioned in Section 3.1, ply angles of 0° primarily act to resist bending. So with divergence occurring in the first bending mode it follows for layup $[0, 0, -45]_S$, outer plies of 0° have a larger influence over divergence than −45° plies. The same conclusion is also drawn from $[90, 90, 45]_S$ layup, as 90° plies primarily counteract twist meaning the majority of bending resistance depends on 45° plies. In the case of $[-45, -45, 45]_S$ where all plies provide resistance from both bending and twist, it is observed the outer plies have the largest impact on divergence. Fig. 11 provides similar conclusions. Soft flutter, being dominated by bending behavior follows the same pattern as the divergence Sobol results. Hard flutter is reached with a twisting mechanism, so the inverse of bending results is observed for Sobol indices.

From the results of the flat plate wing box case study three main conclusions are reached:

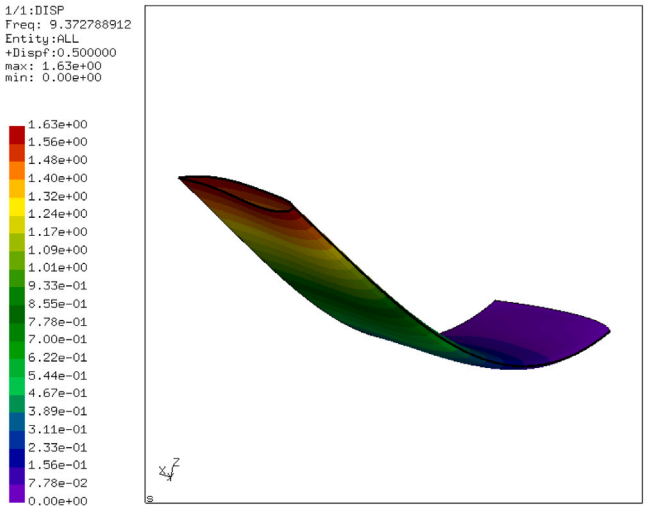

(a) Fist bending mode

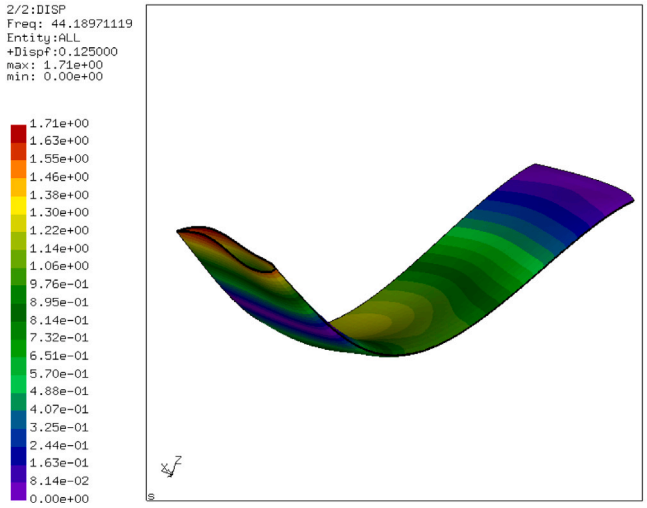

(b) Second bending mode

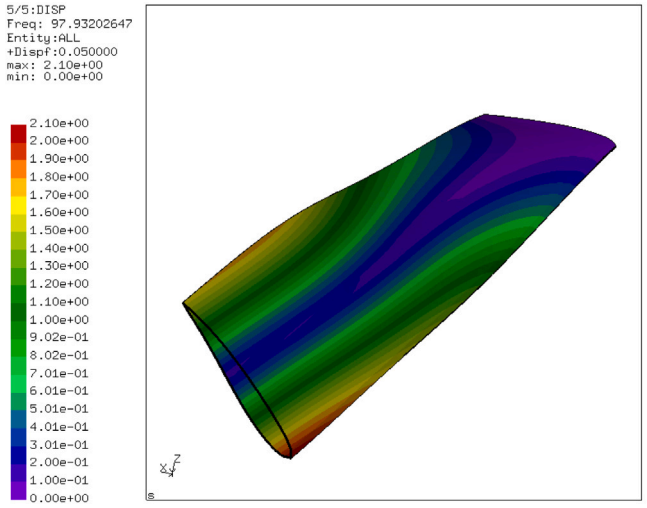

(c) First torsion mode

Fig. 14. Mode shapes of aerofoil shaped wing box model.

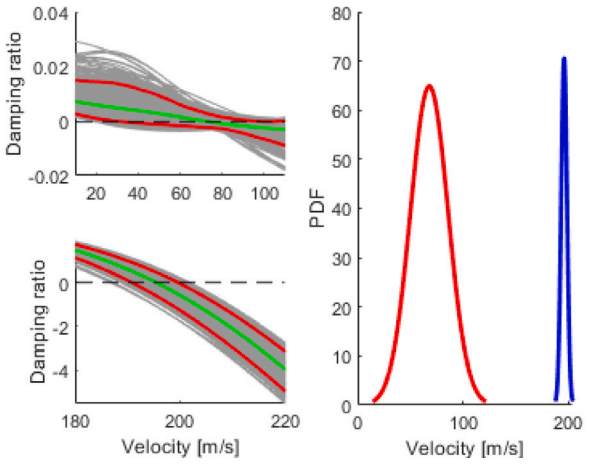

(a) Layup [-45, -45, 45]s

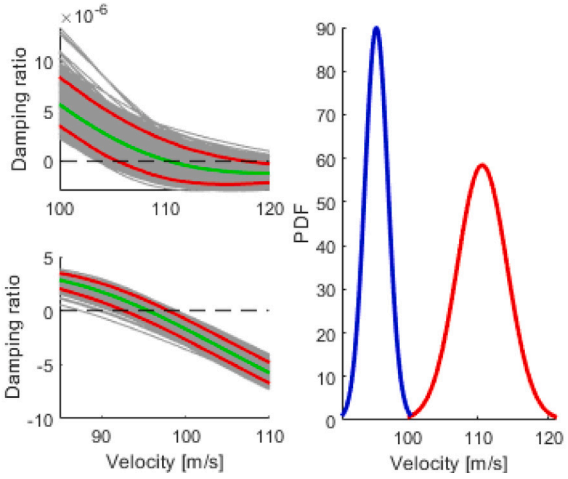

(b) Layup [0, 0, -45]s

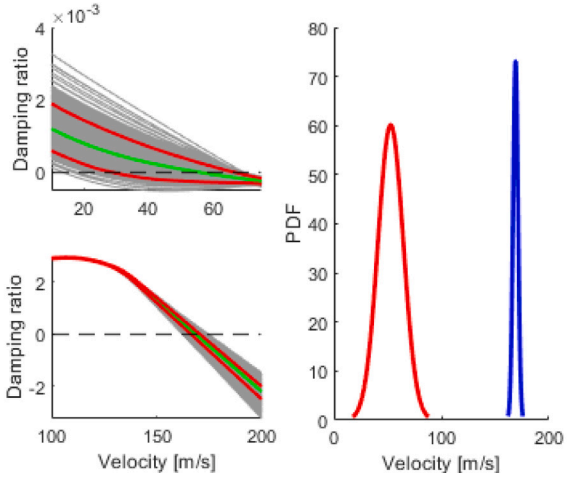

(c) Layup [90, 90, 45]s

Fig. 15. PDF of divergence velocity in aerofoil shaped wing box case study (soft flutter –), (hard flutter –).

1. Attention should be paid to the mechanism by which the mode becomes unstable, building separate surrogate models for each mode
2. Accurate surrogate models can be constructed with the use of Kriging in the flat plate case with under 200 training runs
3. Global sensitivity analysis shows the surrogate models have physical significance

With the methodology validated on a low-fidelity flat plate test case, the benefits can be exploited on a high fidelity aerofoil shaped wing box case study case.

4. Aerofoil shaped wing box case

In this section, aerofoil shaped wing box case study is discussed. First, the model setup is presented and then the results are described and discussed.

4.1. Model setup

For the aerofoil shaped wing box case study, a cantilevered wing model shown in Fig. 12 is generated for the study. The cross-section geometry is based on NACA0012 aerofoil shape and its parameters are shown in Table 4. The structure made of shell elements which CalculiX internally expands to twenty-node brick elements (C3D20). In a composite layup the number of through-thickness bricks corresponds to the number of composite plies. Using the parameters presented in Table 4, this results in 288 000 degrees-of-freedom. Similar to the flat plate case, a symmetrical 6-ply laminate is used for the skin of the wing box. Fig. 14 shows mode shapes that dominate aeroelastic behavior as will be discussed in the following. As opposed to manual construction, the aerofoil shaped wing box model is developed through an automated FEM process through an Open source Python script [53]. This automated process takes place in four steps as follows:

1. Python inputs including the geometry and meshing properties are defined to generate high-fidelity modeling instructions through CalculiX GraphiX.
2. The package is then executed to generate the parametric FE model and output a corresponding regular FEM shell mesh.
3. Composite material input properties are associated with the developed FEM mesh and a normal modal analysis is performed using CalculiX CrunchiX.
4. The undamped modal structural stiffness and mass matrices are derived from the analysis outputs.

With a mesh of the structure, local element mass and stiffness matrices are integrated into global matrices accounting for connections and interactions between elements. To simplify interpretation and analysis of mode shapes a normalization step is carried out. All outputs of the eigenmodes are normalized by means of the generalized mass matrix, where the generalized mass is the same as the modal mass. This means the eigenvectors are scaled such that pre- and post-multiplying the mass matrix by the eigenvectors for each mode results in an identity matrix. Since there is no damping in the model, the eigenvalues of the generalized eigenvalue problem are the squares of the eigenfrequencies. So, the modal stiffness matrix is simply a diagonal matrix of the squared natural frequencies. With structural matrices assembled, aeroelastic analysis can be conducted following the same methodology as the flat plate case. This process still has a high computational cost, meaning directly running thousands of samples for the purpose of uncertainty quantification is still unfeasible with run times ranging from 90–180 s. However, since the process has been automated, it is convenient and feasible to generate certain training data for the development of a surrogate model for the uncertainty quantification. This part will be discussed in the following section. As spanwise geometry of the wing remains unswept and the airspeed is relatively low, a strip theory aerodynamic model is again implemented with the same formulation as in Eq. (21). Aerodynamic matrices are yet again determined implementing incremental work done by the aerodynamic forces over the wing

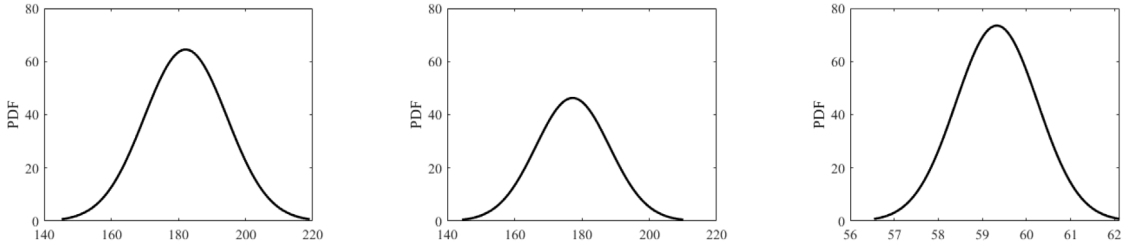

(a) Layup [-45, -45, 45]s (b) Layup [0, 0, -45]s (c) Layup [90, 90, 45]s

Fig. 16. PDF of divergence velocity in aerofoil shaped wing box case study.

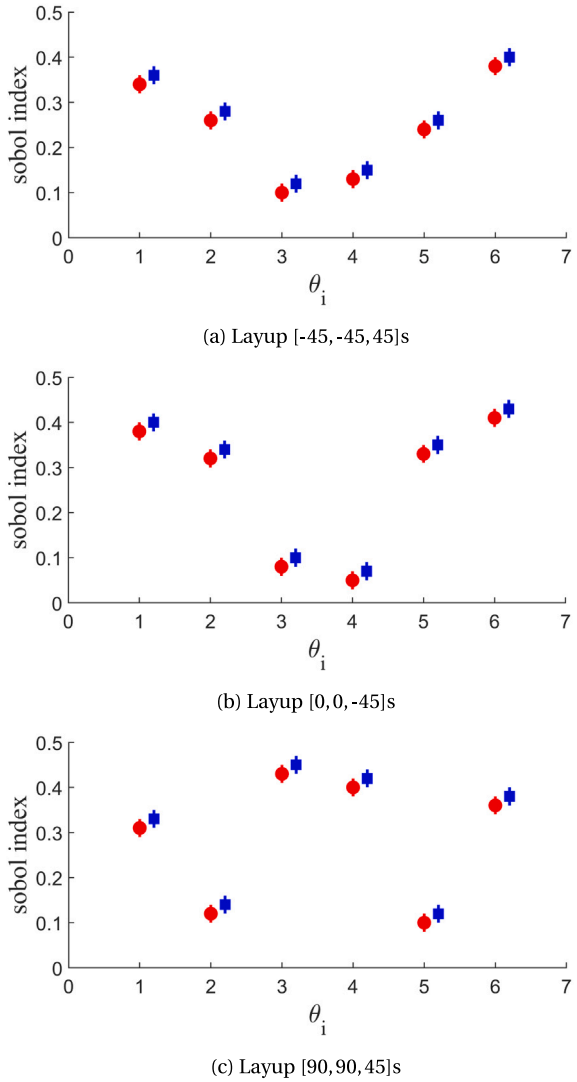

(a) Layup [-45, -45, 45]s

(b) Layup [0, 0, -45]s

(c) Layup [90, 90, 45]s

Fig. 17. Sobol indices for divergence in aerofoil shaped wing box case study.

surface with respect to generalized coordinates. Chordwise rigidity is not assumed as in Appendix B, so the formulation is as follows

$$\rho_{air} V \hat{\mathbf{B}} \dot{q} + \rho_{air} V^2 \hat{\mathbf{C}} q = -\frac{\partial}{\partial q_i} W \tag{23}$$

where W is defined in Eq. (20) and incremental twist and deflections are sums over all k modes

$$w = \sum_{i=0}^{k} q_i w_i$$
$$\chi = \sum_{i=0}^{k} q_i \chi_i \tag{24}$$

4.2. Results

Both soft and hard flutter are observed in two separate modes. Fig. 13 displays damping ratio plots for both modes in the case of a $[-45, -45, 45]$s laminate. The model enters flutter in two modes, one with a sharp gradient three orders of magnitude greater than the other. This indicates a hard flutter mode with a sharp decrease in damping mode and a soft flutter mode with a gradual decrease [52]. Soft flutter occurs before hard flutter as in the flat plate case study, but the modes become unstable further apart by more than 100 m/s.

Table 5 shows the deterministic results from aeroelastic analysis of the aerofoil shaped wing box test case. As was the case in the flat plate study, $[-45, -45, 45]$s laminate has the highest divergence and hard flutter speed. Laminate $[0, 0, -45]$s has the highest soft flutter speed and it reaches hard flutter before the soft flutter. Fig. 14 shows the undamped normal mode shapes of the wing FEM for laminate $[-45, -45, 45]$s. It is obvious that divergence in both cases is characterized by the first bending mode; Soft flutter is in the second bending mode and Hard flutter is dominated by the first torsion mode. The wing is an untapered uniform lifting surface again, so divergence occurs in the first bending mode as opposed to a torsional mode as is typical in tapered wings. Compared to Fig. 5, it is shown similar mode shapes enter divergence and both flutter modes for both test cases. However, the deformation in the aerofoil shape can be observed in Fig. 14 that will not be accounted for in the flat plate case.

Kriging surrogate models are built for each aeroelastic behavior following the methodology described in Section 2.4. The difference between the flat plate wing box study is that the structural model in this aerofoil shaped case is the automated parametric framework is implemented to generate high fidelity structural matrices then CalculiX is used for finite element analysis. The same methodology is applied to construct surrogate models for divergence speed and both flutter modes using the same criteria for convergence. It is found that 200–350 training samples can provide sufficiently accurate surrogate models.

Material uncertainty in the ply orientation angle was then introduced with the same distributions and methodology as in the flat plate case study. Results for mean flutter velocity have converged by 1000 samples using the same criteria as in the flat plate study.

Fig. 15 shows the damping ratio plots for the laminates investigated with the corresponding distributions for flutter speeds subject to material uncertainty. In all three cases, there is no overlap between the behaviors. Upper and lower confidence bands for hard flutter behavior

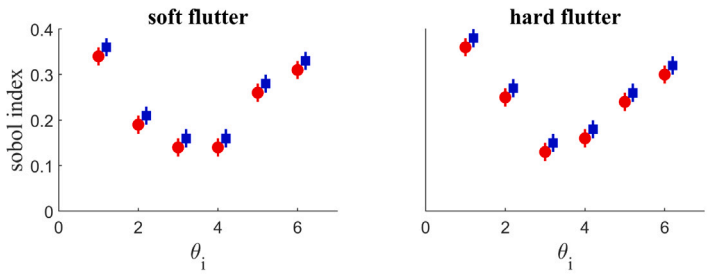

(a) Layup [-45, -45, 45]s

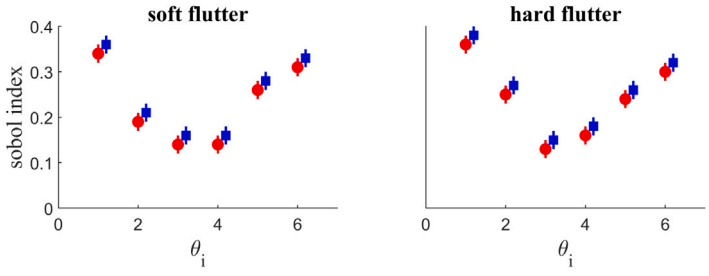

(b) Layup [0, 0, -45]s

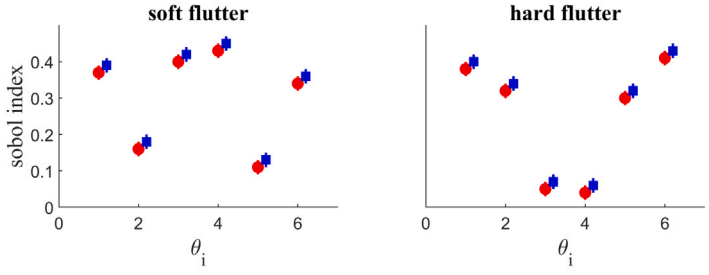

(c) Layup [90, 90, 45]s

Fig. 18. Sobol indices for flutter aerofoil shaped wing box case study.

cross the x-axis in relatively close proximity to each other, with a maximum range of 6 m/s in layup $[0, 0, -45]$s. This results in sharp PDFs for hard flutter when compared to divergence and soft flutter. It is observed that soft flutter modes have wider PDFs when compared to hard flutter. This is potentially due to the shallow gradient approaching zero damping. PDFs related to divergence velocity are shown in Fig. 16, where similar shapes are observed for each laminate following a normal distribution. Laminate $[-45, -45, 45]$s has the largest COV of the layups at 26.25%. This is not the case in the flat plate study. The reason why is unclear at this stage, potentially another mode enters divergence at a similar velocity.

Figs. 17 and 18 show that the global sensitivity analysis comes to the same conclusion as the low-fidelity case. It is observed in behavior dominated by bending, plies of 0° have the highest influence on uncertainty and in the case of twisting behavior, 90° plies have the largest. Where only combinations of 45° and −45° are present, outer plies impact uncertainty on aeroelastic characteristics is higher. Global sensitivity analysis is displayed in Figs. 17 and 18. Comparisons with Figs. 10 and 11 show the same patterns are followed.

5. Comparison

Table 6 shows a comparison of the mean and COV of different flutter and divergence speeds between low- and high-fidelity test cases. Similarities are observed in the robustness of all hard flutter modes being within 0.15–1.4% of each other. Divergence of laminates $[0, 0, -45]$s and $[90, 90, 45]$s have the COV in the same range, falling within 0.4–1.6% of each other. In the case of soft flutter, the flat plate test case is more robust in each laminate. Comparing damping ratio plots of the two case studies shows a shallower gradient approaching zero damping in the aerofoil shaped wing box case, potentially giving rise to higher degrees of uncertainty. The main area of agreement between the two test cases is in the global sensitivity analysis. In each case study, for divergence and soft flutter, plies that counteract bending have a greater impact than plies with fiber angles of 90°. The inverse is true for hard flutter where the twist mode dominates. With an increased training sample data set from a parametric model, it is found the same physical results from a aerofoil shaped wing box case study can be produced at early design stages. While direct comparisons between the case studies cannot be made due to differences in geometry it is worth mentioning the high-fidelity case study has significantly higher COV for soft flutter behavior than the low-fidelity study.

6. Conclusion

The paper proposed an efficient methodology for quantifying manufacturing uncertainties on the aeroelastic characteristics of low- and high-fidelity composite wings. An advanced Kriging method-based surrogate model paired with Latin hypercube sampling was developed to improve the computational efficiency of the UQ. A low-fidelity case study based on a flat composite plate was carried out first to validate the proposed methodology before applying it to a high-fidelity FE-based parametric composite model. Aeroelastic analysis was then performed

Table 6
Comparison of low- and high-fidelity case studies.

Layup		Soft flutter		Hard flutter		Divergence	
		Mean [m/s]	COV [%]	Mean [m/s]	COV [%]	Mean [m/s]	COV [%]
$[-45,-45,45]$ s	Flat plate	132.84	1.07	126.70	0.91	260.89	1.88
	Aerofoil shaped	74.80	21.93	193.96	1.14	186.26	26.25
$[0,0,-45]$ s	Flat plate	176.43	1.55	68.21	1.68	111.13	7.97
	Aerofoil shaped	111.04	3.29	95.58	1.83	176.56	6.36
$[90,90,45]$ s	Flat plate	78.55	3.05	37.5	2.75	67.57	1.23
	Aerofoil shaped	60.04	33.49	168.86	1.39	58.49	1.62

to obtain the flutter and divergence velocities. The Sobol-based global sensitivity analysis was also carried out to identify the impact of uncertainty parameters. The deterministic and stochastic results of both test cases are later compared to identify the limitations of simplified modeling.

The UQ methodology has proved effective and efficient for both low- and high-fidelity cases to successfully obtain stochastic flutter and divergence speeds considering the uncertainty associated with each ply of the laminate. From the flat plate wing box test case, it was observed that a soft and hard flutter mode exists in all layups that can overlap leading to situations where either mode becomes unstable first. The aerofoil shaped wing box case study follows the same behavior having two flutter modes of different intensities. When considering divergence, robustness was consistent in two out of the three laminates considered. Robustness in hard flutter behavior was consistent in both case studies. The largest disagreement in results was found in the soft flutter robustness. In all cases of layouts, it was found that high-fidelity results have significantly larger COV than low-fidelity results.

Global sensitivity analysis has shown with behavior dominated by bending, plies of 0° have the highest influence on uncertainty, in both cases here divergence and soft flutter. In both cases hard flutter is in the first torsion mode where 90° plies have the largest impact on uncertainty. Where only combinations of 45° and −45° are present, outer plies impact uncertainty on aeroelastic characteristics is higher.

In two areas consistency between low- and high-fidelity case studies is found

1. Mechanism by which divergence and flutter exists
2. Global sensitivity analysis

In both cases, divergence occurs in the first bending mode, soft flutter in the second bending mode and hard flutter in the first torsion mode. Inconsistency in results is found in the deterministic results and the degree of uncertainty in the aeroelastic characteristics. Differences in deterministic results can be attributed to changes in dimensions between models. Considering robustness, COV results are in agreement for hard flutter behavior between both cases but flat plate cases are up to ten times more robust for soft flutter. While observing the differences between the test cases, conclusions should not be made based on a comparison due to the significant differences in geometry. Further work should consider a direct comparison between a high-fidelity parametric model and a simplified model. It is unclear if this is due to differences in geometry or increased complexity from the high-fidelity study. The similarities in robustness with divergence and hard flutter behavior may suggest it is due to the increased complexity, but this conclusion cannot be definitively stated based on this study.

With aid of a parametric CACULIX model, it is demonstrated that it is possible to consider material uncertainties in a high-fidelity aerofoil shaped wing box test case at early design stages. Although efficient, the collection of training data for surrogate model development is still computationally expensive. It is recommended that future work should focus more on reducing the training sample size required to speed up this process such as on the use of physics-informed techniques and implementing a more complex aerodynamic model.

Declaration of competing interest

All authors have participated in (a) conception and design, or analysis and interpretation of the data; (b) drafting the article or revising it critically for important intellectual content; and (c) approval of the final version.

This manuscript has not been submitted to, nor is under review at, another journal or other publishing venue.

The authors have no affiliation with any organization with a direct or indirect financial interest in the subject matter discussed in the manuscript.

Data availability

Data will be made available on request.

Acknowledgments

The authors acknowledge the support of the EPSRC Impact Acceleration Account project through the University of Strathclyde (EP/T517938/1), and the technical support from Dapta Ltd. Michael McGurk acknowledges the funding support of the EPSRC Doctoral Training Partnership (DTP) studentship for his PhD study at the University of Strathclyde. The authors are also grateful for the valuable feedback from Dr Liu Yang at the University of Strathclyde.

Appendix A. Laminate derivatives

E11 and v12 are longitudinal modulus. E22 and G12 are transverse modulus.

$$\begin{aligned}\mathbf{Q}_{11} &= \frac{E_{11}}{1-\nu_{12}\nu_{21}};\quad \mathbf{Q}_{12} = \frac{\nu_{12}E_{22}}{1-\nu_{12}\nu_{21}}\\ \mathbf{Q}_{21} &= \frac{\nu_{21}E_{11}}{1-\nu_{12}\nu_{21}};\quad \mathbf{Q}_{22} = \frac{E_{22}}{1-\nu_{12}\nu_{21}};\quad \mathbf{Q}_{66} = G_{12}\end{aligned} \tag{A.1}$$

$$\begin{aligned}\mathbf{Q}^*_{11} &= \mathbf{Q}_{11}\cos^2\theta + 2\left(\mathbf{Q}_{12}+2\mathbf{Q}_{66}\right)\sin^2\theta\cos^2\theta + \mathbf{Q}_{22}\sin^4\theta\\ \mathbf{Q}^*_{22} &= \mathbf{Q}_{11}\cos^2\theta + 2\left(\mathbf{Q}_{12}+2\mathbf{Q}_{66}\right)\sin^2\theta\cos^2\theta + \mathbf{Q}_{22}\cos^4\theta\\ \mathbf{Q}^*_{12} &= \left(\mathbf{Q}_{11}+\mathbf{Q}_{22}-4\mathbf{Q}_{66}\right)\sin^2\theta\cos^2\theta + \mathbf{Q}_{12}\left(\sin^4\theta+\cos^4\theta\right)\\ \mathbf{Q}^*_{66} &= \left(\mathbf{Q}_{11}+\mathbf{Q}_{22}-2\mathbf{Q}_{12}-2\mathbf{Q}_{66}\right)\sin^2\theta\cos^2\theta + \mathbf{Q}_{66}\left(\sin^4\theta+\cos^4\theta\right)\\ \mathbf{Q}^*_{16} &= \left(\mathbf{Q}_{11}-\mathbf{Q}_{22}-2\mathbf{Q}_{66}\right)\cos^3\theta\sin\theta - \left(\mathbf{Q}_{22}-\mathbf{Q}_{12}-2\mathbf{Q}_{66}\right)\cos\theta\sin^3\theta\\ \mathbf{Q}^*_{26} &= \left(\mathbf{Q}_{11}-\mathbf{Q}_{22}-2\mathbf{Q}_{66}\right)\cos\theta\sin^3\theta - \left(\mathbf{Q}_{22}-\mathbf{Q}_{12}-2\mathbf{Q}_{66}\right)\cos^3\theta\sin\theta\end{aligned} \tag{A.2}$$

Appendix B. Legendre polynomials and energy derivatives

Legendre polynomials are defined as

$$L_i(\xi) = \sum_{j=0}^{J}(-1)^j\frac{(2i-2j)}{2^i j\,(i-j)\,(i-2j)}\xi^{i-2j} \tag{B.1}$$

where $J = \frac{i}{2}$ $(i = 0, 2, 4, \ldots)$

Energy derivatives are defined as follows (only applies for chordwise rigidity)

$$\begin{aligned}\frac{\partial(\delta W)}{\partial(\delta q_{i0})} &= -\frac{\pi}{4}\rho_{air}V^2cb\sum_{m=0}^{m_{max}}\int_{-1}^{1}(1+\xi)^4L_m(\xi)L_i(\xi)\\ &\left(1-\left(\frac{\xi+1}{2}\right)^3\right)\left(\frac{\dot{q}_{m0}}{V}+\frac{2q_{m1}}{c}\right)d\xi\\ &= -\begin{bmatrix}\rho_{air}V\hat{\mathbf{B}}_{11} & 0\end{bmatrix}\begin{bmatrix}\dot{\mathbf{q}}_{i0}\\ \dot{\mathbf{q}}_{i1}\end{bmatrix}-\begin{bmatrix}0 & \rho_{air}V^2\hat{\mathbf{C}}_{12}\end{bmatrix}\begin{bmatrix}\mathbf{q}_{i0}\\ \mathbf{q}_{i1}\end{bmatrix}\end{aligned} \tag{B.2}$$

$$\begin{aligned}\frac{\partial(\delta W)}{\partial(\delta q_{i1})} &= \frac{1}{4}\rho_{air}V^2cb\sum_{m=0}^{m_{max}}\int_{-1}^{1}(1+\xi)^4L_m(\xi)L_i(\xi)\\ &\left[\frac{\pi}{2}\left(1-\left(\frac{\xi+1}{2}\right)^3\right)\left(\frac{\dot{q}_{m0}}{V}+\frac{2q_{m1}}{c}\right)+M_{\dot{x}}\left(\frac{\dot{q}_{m1}}{2V}\right)\right]d\xi\\ &= -\begin{bmatrix}\rho_{air}V\hat{\mathbf{B}}_{21} & \rho_{air}V\hat{\mathbf{B}}_{22}\end{bmatrix}\begin{bmatrix}\dot{\mathbf{q}}_{i0}\\ \dot{\mathbf{q}}_{i1}\end{bmatrix}-\begin{bmatrix}0 & \rho_{air}V^2\hat{\mathbf{C}}_{22}\end{bmatrix}\begin{bmatrix}\mathbf{q}_{i0}\\ \mathbf{q}_{i1}\end{bmatrix}\end{aligned} \tag{B.3}$$

$\hat{\mathbf{B}}_{11}$, $\hat{\mathbf{B}}_{21}$, $\hat{\mathbf{B}}_{22}$, $\hat{\mathbf{C}}_{12}$ and $\hat{\mathbf{C}}_{22}$ are extracted as the square sub-matrices of aerodynamic damping and stiffness matrices $\hat{\mathbf{B}}$ and $\hat{\mathbf{C}}$ [54].

$$\hat{\mathbf{B}}=\begin{bmatrix}\hat{\mathbf{B}}_{11} & 0_{N\times N}\\ \hat{\mathbf{B}}_{21} & \hat{\mathbf{B}}_{22}\end{bmatrix}\qquad \hat{\mathbf{C}}=\begin{bmatrix}0_{N\times N} & \hat{\mathbf{C}}_{12}\\ 0_{N\times N} & \hat{\mathbf{C}}_{22}\end{bmatrix}$$

References

[1] Dray L, Schäfer AW, Grobler C, Falter C, Allroggen F, Stettler ME, Barrett SR. Cost and emissions pathways towards net-zero climate impacts in aviation. Nature Clim Change 2022;12(10):956–62.

[2] Timmis AJ, Hodzic A, Koh L, Bonner M, Soutis C, Schäfer AW, Dray L. Environmental impact assessment of aviation emission reduction through the implementation of composite materials. Int J Life Cycle Assess 2015;20:233–43.

[3] Wright JR, Cooper JE. Introduction to aircraft aeroelasticity and loads, Vol. 20. John Wiley & Sons; 2008.

[4] Board CA. Investigation of aircraft accident: BRANIFF airways: BUFFALO, TEXAS: 1959-09-29. 1959.

[5] Stodieck O, Cooper J, Weaver P, Kealy P. Aeroelastic tailoring of a representative wing box using tow-steered composites. AIAA J 2017;55(4):1425–39.

[6] Scarth C, Cooper JE, Weaver PM, Silva GH. Uncertainty quantification of aeroelastic stability of composite plate wings using lamination parameters. Compos Struct 2014;116:84–93.

[7] Stodieck O, Cooper JE, Weaver PM, Kealy P. Improved aeroelastic tailoring using tow-steered composites. Compos Struct 2013;106:703–15.

[8] Marano AD, Belardo M, Beretta J, Starace F, Orlando S, Punzi C, Frajese R, Paletta N, Di Palma L. Aeroelastic tailoring of the next generation civil tiltrotor technological demonstrator composite wing. Aerospace 2022;9(7):335.

[9] Rajpal D, Mitrotta F, Socci C, Sodja J, Kassapoglou C, De Breuker R. Design and testing of aeroelastically tailored composite wing under fatigue and gust loading including effect of fatigue on aeroelastic performance. Compos Struct 2021;275:114373.

[10] Zheng Y, Wang Y. Flutter stability analysis of aeroelastic systems with consideration of hybrid uncertain parameters. Mech Syst Signal Process 2023;185:109782.

[11] Mesogitis T, Skordos AA, Long A. Uncertainty in the manufacturing of fibrous thermosetting composites: A review. Composites A 2014;57:67–75.

[12] Li L. Structural design of composite rotor blades with consideration of manufacturability, durability, and manufacturing uncertainties (Ph.D. thesis), Georgia Institute of Technology; 2008.

[13] Dodwell TJ, Kynaston S, Butler R, Haftka RT, Kim NH, Scheichl R. Multilevel Monte Carlo simulations of composite structures with uncertain manufacturing defects. Probab Eng Mech 2021;63:103116.

[14] Esposito M, Gherlone M. Material and strain sensing uncertainties quantification for the shape sensing of a composite wing box. Mech Syst Signal Process 2021;160:107875.

[15] Oh D, Librescu L. Free vibration and reliability of composite cantilevers featuring uncertain properties. Reliab Eng Syst Saf 1997;56(3):265–72.

[16] Khan B, Potter K, Wisnom M. Suppression of delamination at ply drops in tapered composites by ply chamfering. J Compos Mater 2006;40(2):157–74.

[17] Georgiou G, Manan A, Cooper JE. Modeling composite wing aeroelastic behavior with uncertain damage severity and material properties. Mech Syst Signal Process 2012;32:32–43.

[18] Zhou X-Y, Ruan X, Gosling P. Robust design optimization of variable angle tow composite plates for maximum buckling load in the presence of uncertainties. Compos Struct 2019;223:110985.

[19] Stodieck O. Parametric FEM model creation with python and calculix graphix (cgx). 2021, URL https://www.dapta.com/dynamic-aeroelastic-flutter-and-divergence-analysis-with-python-and-calculix-crunchix/.

[20] Kilimtzidis S, Kostopoulos V. Static aeroelastic optimization of high-aspect-ratio composite aircraft wings via surrogate modeling. Aerospace 2023;10(3):251.

[21] Rumpfkeil MP, Beran P. Multi-fidelity surrogate models for flutter database generation. Comput & Fluids 2020;197:104372.

[22] Santhanam C, Riva R, Knudsen T. Surrogate models for predicting stall-induced vibrations on wind turbine blades. In: Journal of physics: Conference series, Vol. 2265. IOP Publishing; 2022, 032005.

[23] Ni P, Li J, Hao H, Xia Y, Du X. Stochastic dynamic analysis of marine risers considering fluid-structure interaction and system uncertainties. Eng Struct 2019;198:109507.

[24] Sudret B. Global sensitivity analysis using polynomial chaos expansions. Reliab Eng Syst Saf 2008;93(7):964–79.

[25] Avendano-Valencia LD, Chatzi EN, Tcherniak D. Gaussian process models for mitigation of operational variability in the structural health monitoring of wind turbines. Mech Syst Signal Process 2020;142:106686.

[26] Giovanis DG, Shields MD. Data-driven surrogates for high dimensional models using Gaussian process regression on the grassmann manifold. Comput Methods Appl Mech Engrg 2020;370:113269.

[27] Ni P, Li J, Hao H, Han Q, Du X. Probabilistic model updating via variational Bayesian inference and adaptive Gaussian process modeling. Comput Methods Appl Mech Engrg 2021;383:113915.

[28] Yan W-J, Chronopoulos D, Papadimitriou C, Cantero-Chinchilla S, Zhu G-S. Bayesian inference for damage identification based on analytical probabilistic model of scattering coefficient estimators and ultrafast wave scattering simulation scheme. J Sound Vib 2020;468:115083.

[29] Liu Y, Wang X, Wang L. A dynamic evolution scheme for structures with interval uncertainties by using bidirectional sequential kriging method. Comput Methods Appl Mech Engrg 2019;348:712–29. http://dx.doi.org/10.1016/j.cma.2019.01.041.

[30] McKay M, Beckman R, Conover W. Acomparison of three methods for selecting values of inputvariables in the analysis of output from a computer code. Technometrics 1979;21(2):239–45.

[31] Sharifi M, Vincenti A, Chassaing J-C. Aeroelastic optimisation of composite structures in aeronautics. In: 15ème colloque national en calcul des structures. 2022.

[32] Zhang B, Wang Q, Liu X, Zu L, Yuan H. Aeroelastic optimization design of composite materials blade based on RBF/ROM and CCA reliability analysis. Compos Struct 2022;300:116162.

[33] Sobol IM. Global sensitivity indices for nonlinear mathematical models and their Monte Carlo estimates. Math Comput Simul 2001;55(1–3):271–80.

[34] Saltelli A, Ratto M, Andres T, Campolongo F, Cariboni J, Gatelli D, Saisana M, Tarantola S. Global sensitivity analysis: the primer. John Wiley & Sons; 2008.

[35] Yuan J, Fantetti A, Denimal E, Bhatnagar S, Pesaresi L, Schwingshackl C, Salles L. Propagation of friction parameter uncertainties in the nonlinear dynamic response of turbine blades with underplatform dampers. Mech Syst Signal Process 2021;156:107673.

[36] Saltelli A. Making best use of model evaluations to compute sensitivity indices. Comput Phys Commun 2002;145(2):280–97.

[37] An open source initiative for the treatment of uncertainties, risks'N statistics. OpenTURNS 2022. URL https://openturns.github.io/www/index.html.

[38] Collar A, Simpson A. Matrices and engineering dynamics. Aeronaut J 1988.

[39] Jacobi CGJ. De determinantibus functionalibus. J Reine Angew Math (Crelles J) 1841;1841(22):319–59.

[40] Bert CW. Classical lamination theory. In: Manual on experimental methods for mechanical testing of composites. Springer; 1989, p. 11–6.

[41] Wei P, Lu Z, Song J. Regional and parametric sensitivity analysis of sobol indices. Reliab Eng Syst Saf 2015;137:87–100.

[42] Cressie N. The origins of kriging. Math Geol 1990;22:239–52.

[43] Van Beers WC, Kleijnen JP. Kriging for interpolation in random simulation. J Oper Res Soc 2003;54:255–62.

[44] Langhaar HL. Energy methods in applied mechanics. Courier Dover Publications; 2016.

[45] Wu Z, Raju G, Weaver PM. Comparison of variational, differential quadrature, and approximate closed-form solution methods for buckling of highly flexurally anisotropic laminates. J Eng Mech 2013;139(8):1073–83.

[46] Whitney JM. Structural analysis of laminated anisotropic plates. CRC Press; 1987.

[47] Al-Obeid A, Cooper J. A Rayleigh–Ritz approach for the estimation of the dynamic properties of symmetric composite plates with general boundary conditions. Compos Sci Technol 1995;53(3):289–99.

[48] Yates Jr EC. Modified-strip-analysis method for predicting wing flutter at subsonic to hypersonic speeds. J Aircr 1966;3(1):25–9.
[49] Hancock GJ. An introduction to the flight dynamics of rigid aeroplanes. 1995.
[50] Hodges DH, Pierce GA. Introduction to structural dynamics and aeroelasticity, Vol. 15. cambridge University Press; 2011, p. 139–63.
[51] Shixiong Z, Junfeng G, Yu Z. Characteristics and suppression measures for soft flutter of main girder with Π -shaped cross section. J Southwest Jiaotong Univ 2017;52(3).
[52] Kelley CL, Paquette J. Investigation of flutter for large, highly flexible wind turbine blades. In: Journal of physics: Conference series, Vol. 1618. IOP Publishing; 2020, 052078.
[53] Stodieck O. Dynamic aeroelastic flutter and divergence analysis with python and calculix. Dapta LTD 2022. URL https://github.com/daptablade/parametric_cgx_model.
[54] Stodieck O. Aeroelastic tailoring of tow-steered composite wings (Ph.D. thesis), University of Bristol; 2016.